Unloading of elastoplastic spheres from large deformations

B. D. Edmans*, I. C. Sinka

University of Leicester, University Road, Leicester LE1 7RH, United Kingdom

Abstract

The unloading behaviour of adhesion-free elastic-perfectly plastic spheres following contact presents complex non-linear features. Analytical models capable of accurately predicting this response have not yet been developed for an extensive range of material properties and initial deformation states, and consequently the use of semi-empirical models requiring calibration is widespread in the practical application of contact laws.

In this work, we provide insight into contact behaviour during unloading by conducting a finite element study to characterise this response for a comprehensive range of material properties ($1 \leq E/\sigma_y \leq 1000$, $0.0 \leq \nu \leq 0.45$) and for particles that have undergone large deformation prior to unloading ($0.01 \leq d/R \leq 0.5$), leading to the following findings. Firstly, an empirical relation capable of accurately determining secant unloading stiffness from material properties and degree of initial deformation was formulated, which was expressed in non-dimensional form for maximum generality. An analytical model was also developed to help explain some of the contributing mechanisms identified from the finite element analysis. Secondly, the nonlinearity of the force-displacement curve in unloading was quantified and charted, and physical arguments were advanced to explain the trends revealed. Considering both stiffness and nonlinearity results, it was concluded that a single synthetic measure of initial particle deformation relative to deformation at first yield, which is currently used, is insufficient to characterise unloading response at large displacements.

The unloading relations developed can be employed with static and dynamic multi-particle simulation approaches such as the Discrete Element Method (DEM) for more accurate simulation of compaction and flow of dense powder beds and problems reliant on accurate determination of contact areas after unloading between particles following large deformation.

Keywords: Contact laws, Unloading, Large displacement, Elastoplastic particles, Particle mechanics

*Corresponding author. Email: `bde2@leicester.ac.uk`

1. Introduction

In the absence of adhesive forces, the unloading of a plastically deformed sphere in contact with a rigid surface is predominantly elastic, yet typically shows nonlinear load-displacement behaviour. In many practical cases, separation occurs at relatively small withdrawal displacements and is associated with little elastic relaxation. With increasing use of multiparticle simulation techniques such as the Discrete Element Method (DEM) [1] and extensions incorporating larger particle deformations, nonlocal contact [2] and interparticle bonds (for example, Potyondy and Cundall [3]), the development of accurate models for particle unloading is desirable. A survey of models proposed for the adhesionless, rate-independent unloading of spherical particles is provided below.

Analytical models describing the response of spherical particles were first provided by Hertz [4] for elastic spheres subject to small deformations. Tatara [5] provided analytical relations for large displacements of elastic spheres, with emphasis on describing the radial displacement field. An analytical treatment of plastic deformation in the contact problem was developed by Hill [6] using slip line theory. The concept of self-similarity was developed by Storåkers [7] et al. to obtain solutions for a range of inelastic contact problems. Mesarovic and Johnson [8] developed a detailed analytical model for loading of elastic-plastic-adhesive particles, which was used to develop regime maps of the particle response. An analytical model that blends elastic and plastic response was developed by Brake [9] in which plastic deformation is understood as modifying the effective radius of curvature that is used in the Hertzian load-displacement relation used to describe unloading. The model was shown to describe loading/unloading response accurately at small displacements. A synthetic model for contact force as a function of contact area incorporating bond strength was presented by Gonzelez et al. [10], incorporating relations from Mesarovic and Johnson's [8] model.

Semi-empirical particle contact models described by piecewise load-unload curves have been developed by a number of authors (for example, Pasha et al. [11]) for multiparticle simulations, often starting from the concept of linearised response with distinct values stiffness for loading and unloading. A detailed survey of such models, including a variety of physical phenomena (such as elasticity, plasticity, viscosity, adhesion and others), including relations for unloading, was provided by Tomas [12]. The increase in unloading stiffness with increasing particle deformation was recognised by Luding [13], whose model allows for a linear increase with deformation for deformations exceeding a critical value in a comprehensive contact model developed for DEM simulations. Walton and Braun [14] proposed that unloading stiffness (defined as maximum load divided by recovered displacement) has a linear relationship to unloading maximum force before unloading. Thakur et al. [15] assume a constant value for unloading stiffness but propose a power-law force-displacement relation in unloading.

The unloading response of particles has also been described dynamically in terms of the coefficient of restitution. An analytical model for the dependence of the coefficient of restitution of elastoplastic spheres on the ratio of impact velocity and velocity required to cause yielding was developed by Thornton [16], Thornton and Ning [17] and Stronge [18]. Corresponding numerical studies involving large particle deformations were conducted by Li et al. [19] using the Material Point Method.

Numerical studies have been used to investigate the static unloading response of spheres. Systematic, parametric finite element studies exploring the indentation of elastoplastic spheres with power-law hardening were conducted by Alcala [20]. Load-displacement relations for loading and unloading of spheres following plastic deformation have been proposed by Etsion et al. [21] based on finite element studies using a variety of values for elastic stiffness and yield strength. Olsson and Larsson [22] conducted finite element studies of loading and unloading of elastic-plastic spheres with adhesion and power-law hardening for displacements up to 10% of the particle initial radius. Rathbone et al. used finite element studies to establish the magnitude of an effective curvature for a Hertzian unloading response as a function of Poisson's ratio and displacement before unloading, for spheres subject to small deformations. Finite element studies were conducted by Rojek et al. [23] to determine the unloading response of metal spheres, described by a power-law hardening plasticity model, for a wide range of displacements, concluding that the linear Walton-Braun relationship between dimensionless load and dimensionless displacement is sufficiently accurate, and that unloading stiffness (defined as maximum load before unloading divided by recovered displacement) has a linear dependence on dimensionless displacement. Recognising the importance of contact area development for particle load-displacement response, Vu-Quoc et al. [24] developed an incremental algorithm for elasto-plastic contact based on tracking the development of total and plastic contact area, which was calibrated using finite element simulations and shown to be accurate for small displacements. However, the literature to date does not include a method for determining unloading stiffness for an extensive space of material properties and large deformations prior to unloading.

The structure of this article is as follows: in Section 2, a power-law law model is identified for the evaluation of force-displacement behaviour in unloading, introducing two parameters, ρ and α, representing secant unloading stiffness and nonlinearity, respectively. In Section 3, the finite element simulations used to generate loading/unloading data are described. In Section 4, results, including both particle forces and contact area, are analysed. Section 5 introduces a simplified analytical model of unloading that captures the prominent features in the full finite element results. Discussion and conclusions are presented in Sections 6 and 7, respectively.

2. Framework

2.1. Definitions

In this article, relationships between particle load and displacement are developed in dimensionless form for maximum generality, particle load being normalised with respect to yield stress and initial projected area ($\bar{F} = F/\pi R_0^2 \sigma_y$) and geometrical/kinematic quantities (displacement and contact radius) being normalised with respect to the initial radius ($\bar{\delta} = \delta/R_0$, $\bar{a} = a/R_0$). Dimensionless material stiffness ($\bar{E}$) is obtained by dividing Young's modulus by yield strength (σ_y). $\bar{E}$ is thus the inverse of the strain at first yield in a constant-section, linear elastic bar. Consequently, particles with high $\bar{E}$ will yield at low values of $\bar{\delta}$, their response will be mostly plastic and little displacement will be recovered on unloading, whereas for the lowest values of $\bar{E}$, no yielding will occur and the full displacement incurred will be recovered.

For a given particle load prior to unloading, it is convenient to express the unloading stiffness in terms of the displacement of the particle centre before unloading and the displacement at which the particle separates from the surface. Using $\bar{\delta}_{max}$ as the dimensionless particle displacement at the start of unloading and $\bar{\delta}_0$ as the corresponding value at separation, the stiffness measure ρ is defined using Eq. 1. These quantities are illustrated in Fig. .1.

$$\rho = \frac{1}{\bar{\delta}_{max} - \bar{\delta}_0} \tag{1}$$

Considering that the Hertz analytical solution for contact of elastic spheres is a power law, and that the results from the current study are expected to approach the Hertz solution as $\bar{E}$ and $\bar{\delta}_0$ tend to zero, it is reasonable to consider that unloading response of deformed spheres where the assumptions of the Hertz law are progressively relaxed will be of a similar form. It is thus assumed that the force-displacement response of a particle during unloading can be described by a simple two-parameter power-law model (Eq. 2).

$$\bar{F}(\bar{\delta}) = \begin{cases} 0, & \bar{\delta} \leq \bar{\delta}_0 \\ \bar{F}_{max} \left(\frac{\bar{\delta} - \bar{\delta}_0}{\bar{\delta}_{max} - \bar{\delta}_0} \right)^{\alpha}, & \bar{\delta} > \bar{\delta}_0 \end{cases} \tag{2}$$

This two-parameter form allows the intuitive concepts of stiffness and nonlinearity in unloading response to have simple mathematical expression, simplifying their independent investigation. The exponent α is a measure of the nonlinearity of the unloading, which is 1.5 in the case of unloading following the classical Hertz law. It is noted that Eq. 2 is identical to the unloading relation proposed by Etsion et al. [21]. If $\bar{F}_{max}$ and $\bar{\delta}_{max}$ are available from an incremental procedure (such as DEM) and ρ and α can be estimated by an appropriate model, such as that developed in the current work, the separation displacement $\bar{\delta}_0$ is obtained by rearranging Eq. 1 and the load-displacement response (Eq. 2) can be computed. Characteristic unloading responses calculated using the power law are illustrated in Fig. .1. In the following, appropriate functional forms for $\alpha = \alpha(\bar{E},\ \nu,\ \bar{\delta}_{max})$ and $\rho = \rho(\bar{E},\ \nu,\ \bar{\delta}_{max})$ will be developed.

[Figure 1 about here.]

3. Numerical simulations

Systematic finite element studies were carried out using the commercial finite element analysis software Abaqus 6.14-1 to establish particle unloading response under a wide range of conditions. An axisymmetric finite element model of a sphere contacting a rigid surface was created implementing an elastic-von Mises perfectly plastic material model, with 6670 quadrilateral axisymmetric elements in a mapped mesh (Fig. .2). The mesh was progressively refined towards the contact surface such that each element edge along the sphere surface in the refined sector occupies 11.25 minutes of arc. Values of 1, 2, 5, 10, 20, 50, 100, 200, 500 and 1000 were used for the stiffness ratio $\bar{E}$, values of 0.0, 0.15, 0.30 and 0.45 were used for the Poisson's ratio ν, and values of 0.01, 0.02, 0.03, 0.04, 0.05, 0.1, 0.15, 0.2, 0.25, 0.3, 0.35, 0.4, 0.45, 0.5 were used for the dimensionless displacement at the start of unloading. Testing all combinations of parameters resulted in a total of 560 simulations. A frictionless contact interaction was prescribed. Nodes on the particle midsurface were constrained to have the same axial displacement throughout the simulation. Displacement control was used during the loading step. During the unloading step, the displacement constraint was released and reaction forces were ramped linearly to zero, generating results at 100 equally-spaced load steps, each with nonzero total particle load, for all simulations conducted.

[Figure 2 about here.]

4. Numerical results

4.1. Load-unload behaviour

Selected load-unload curves obtained from the simulations (those with $\nu = 0.3$) are shown in Fig. .3.

[Figure 3 about here.]

As $\bar{E}$ increases, the plastic zone development changes. For the lowest value of $\bar{E}$ (1), no yielding occurs in the range of deformations investigated. The points of first yield for the loading step of each simulation are indicated by circles in Fig. .3. For $\bar{E} < 5$, yielding first occurs at the particle centre. For $5 \leq \bar{E} \leq 20$, yielding first occurs from the point on the axis of loading somewhat below the surface, as predicted by linear elastic theory (see, for example, Timoshenko and Goodier [25]). For $50 \leq \bar{E} \leq 200$, the developing plastic zone interacts with the contact surface and for the stiffest particles ($\bar{E} > 500$), yielding first occurs at the contact surface, almost immediately after contact is established. When plastic flow becomes the dominant deformation mechanism in the particle, increase in particle load with deformation is retarded, as further increase in load-bearing capacity is dependent on increase in contact area alone. Consequently, a relation can be observed between displacements corresponding to the minima of the gradients of the curves in Fig. .3 and the values of displacement at which strain energy maxima are attained (Fig. .4). Similar results are obtained for other values of ν.

Unloading is primarily elastic, though some plastic flow was observed during unloading in simulations with high $\bar{E}$.

[Figure 4 about here.]

4.2. Determination of parameters of unloading relation

As the displacement at particle separation ($\bar{\delta}_0$) was considered prescribed by the terminal state of the simulations, a one-parameter Newton-Raphson procedure was used to determine the value of α that minimised the error between FE results and the proposed unloading relation (Eq. 2). The median value of the coefficient of determination (R^2) across 560 simulations was 0.999847, which supports the choice of the unloading relation in power-law form.

4.3. Results for unloading stiffness (ρ)

Inspection of variation of unloading stiffness (ρ) results with material stiffness ($\bar{E}$) and displacement before unloading ($\bar{\delta}_{max}$) for $\nu = 0.3$ (Figs. .5 and .6, respectively) suggests how unloading stiffness can be related to these variables.

[Figure 5 about here.]

[Figure 6 about here.]

Inspection of Fig. .5 suggests that a two-part, constant-linear relation between ρ and $\bar{E}$ can provide a good approximation to the simulation results, providing a simple link between the material stiffness and unloading stiffness. After introducing a function (ϕ) that blends between responses from elastic and plastically deformed particles and a term accounting for variation due to Poisson's ratio, a general model function (Eq. 3) was developed,

$$\rho(\bar{E},\ \nu,\ \bar{\delta}_{max}) \approx \frac{1}{\bar{\delta}_{max}} + \phi\bar{E}\left(\gamma_1\bar{\delta}_{max} + \gamma_2\bar{\delta}_{max}^{-\gamma_3} + \gamma_4\nu\right) \tag{3}$$

with the supplementary functions ϕ and $\bar{\delta}_c$ defined by Eqs. 4 and 5,

$$\phi = H(\bar{\delta}_{max} - \bar{\delta}_c)\left(1 - \frac{\bar{\delta}_c}{\gamma_5\bar{\delta}_{max} + (1-\gamma_5)\bar{\delta}_c}\right) \tag{4}$$

$$\bar{\delta}_c(\bar{E},\nu) = \left(\frac{2.8\pi(0.454\nu + 0.41)(1-\nu^2)}{2\bar{E}}\right)^2 \tag{5}$$

where $H(\cdot)$ is the Heaviside step function and $\bar{\delta}_c$ is the dimensionless displacement at first yield, a well-established approximation (see Etsion et al. [21], Chang et al. [26]) which shows good agreement with values obtained from the current simulations, as shown in Fig. .7. The second term in brackets in Eq. 4 represents a one-parameter family of blending functions $\psi : \mathbb{R}^+ \to [0,1]$, with the properties $\psi(0) = 0$, $\psi'(0) \neq 0$, $\lim_{x\to\infty} \psi(x) = 1$ and $\lim_{x\to\infty} \psi'(x) = 0$.

[Figure 7 about here.]

This model allows two types of behaviour to be distinguished: at small displacements, and for models with low $\bar{E}$, unloading is fully elastic; the recovered strain proportion is unity (independent of $\bar{E}$), so that Eq. 1 reduces to $\rho = 1/\bar{\delta}_{max}$. Conversely, once plastic deformation has occurred, the unloading stiffness increases with increasing material stiffness. The decay term $\gamma_2\bar{\delta}_{max}^{-\gamma_3}$ represents the phenomenon visible in Fig. .6 that unloading stiffness is increased at small values of $\bar{\delta}_{max}$. The presence of this term indicates an asymmetry in the influence of increasing material stiffness and increasing initial displacement on the unloading response; a phenomenon that is not captured by models in which the unloading response depends on $\bar{\delta}/\bar{\delta}_c$, such as those described by Etsion et al. [21].

A optimization algorithm was used to find parameters values that minimized the total absolute error between the calculated values of secant stiffness and those obtained from the FE simulations. The parameters of best fit are shown in Table .1. The median, 75th, 90th and 100th percentile relative errors between the results of the calibrated model and the FE data were 1.84%, 5.29%, 11.78% and 36.33%, respectively. Full comparisons between the model and FE results are shown in Fig. .19.

[Table 1 about here.]

It is noted the influence of ν on results, represented by the parameter γ_4, is relatively minor, as can be appreciated by inspecting Figs. .21 and .22 in the Appendix.

4.4. Results for unloading nonlinearity (α)

Results for α obtained from the simulations are shown in Figs. .8a and .8b, for large and small displacements, respectively, for $\nu = 0.30$, while full results for all simulations are shown in the Appendix (Fig. .20).

[Figure 8 about here.]

An increase in nonlinearity with deformation is noted for elastic and near-elastic particles ($\bar{E} = 1,\ 2$), to values much greater than that predicted by the Hertz law. Conversely, a reduction in nonlinearity is observed for plastic particles, which reduces further with increasing initial displacement, until the unloading response is nearly linear. The trends in unloading nonlinearity can be explained with reference to contact area reduction during unloading and three-dimensional stress states within the solid body.

Firstly, the unloading response of a yielded, linear elastic, prismatic bar without lateral constraints at small displacements is linear ($\alpha = 1$); the contact area remains constant during unloading and the stress state of the bar is uniform and reduces linearly with reducing axial strain to zero.

Secondly, the response of a fully elastic sphere ($\bar{E} = 1$), the unloading nonlinearity exponent is 1.5 as displacement before unload ($\bar{\delta}_{max}$) tends to zero, in accordance with Hertz theory. As $\bar{\delta}_{max}$ increases, α increases as the assumptions of the Hertz model become increasingly inaccurate. In particular, the kinematic assumption in the Hertz law is (dimensionless contact area)$^2 = \bar{\delta}$ whereas the current results show that this increases to about (dimensionless contact area)$^2 = 1.4\bar{\delta}$ at $\bar{\delta} = 0.5$. Upon unloading, the contact area reduces more rapidly than in the Hertz model and nonlinearity of the unloading curve is greater.

Thirdly, when considering the response at high $\bar{E}$ ($\bar{E} = 1000$), when using a von Mises – perfectly plastic material model, admissible yielded stress states may exhibit any value of hydrostatic stress. In cases where a particle is loaded far beyond its point of first yield, increasing load in the contact normal direction drives the stress states out along the yield surface in the direction of increasingly compressive hydrostatic stress to maintain equilibrium. In addition, the stress state in the body becomes more uniform. Unloading from stress states with a large hydrostatic component generally requires volumetric expansion and the cumulative effect of disparate expansions is to limit the amount of kinematic relaxation (and hence reduction in contact area) that can occur during unloading. Consequently, as $\bar{\delta}_{max}$ and $\bar{E}$ increase, the unloading approaches the conditions present in unloading of a constant-section bar and α tends towards 1.0, although increasing Ebar has a progressively smaller effect.

Finally, it is noted $\bar{E}$ is the primary parameter governing the transition between the behaviours exhibited by the elastic sphere and the constant section bar, the effect of increasing $\bar{\delta}_{max}$ is to magnify the differences in the behaviour, as can be seen in Fig. .8a. The asymmetry in the influence of $\bar{E}$ and $\bar{\delta}_{max}$ supports the conclusion from Section 4.2 that unloading response cannot be characterised by a single measure such as $\bar{\delta}_{max}/\bar{\delta}_c$.

The effects of Possion's ratio on the nonlinearity, as shown in Fig. .22b , are consistent with this explanation: increasing Poisson ratio increases the contact area for the elastic cases, leading to an increase in α, while an increase at high values of $\bar{E}$ decreases α somewhat as internal constraints on volumetric expansion increase as the material tends towards elastic incompressibility.

4.5. Comparisons with other models

Considering firstly, relations for unloading nonlinearity, Etsion et al. [21] proposed the following relation for α (Eq. 6),

$$\alpha(\bar{\delta}_{max}, \bar{E}, \nu) = 1.5 \left(\frac{\bar{\delta}_{max}}{\bar{\delta}_c(\bar{E}, \nu)} \right)^{-0.0331} \tag{6}$$

based on finite element studies at small displacements, where $\bar{\delta}_c$ is the displacement at first yield, calculated using Eq. 5. Eq. 6 predicts that nonlinearity of the unloading response (α) should decrease monotonically for all values of $\bar{E}$ as the initial displacement increases. However, results from the current study suggest divergent behaviour for low and high values of $\bar{E}$, as described in the previous subsection. This discrepancy is attributed to the fact that Eq. 6 was obtained from fitting of FE results with $297 \leq \bar{E} \leq 2464$ and thatthe response of particles with lower values of $\bar{E}$ was not captured. This suggestion is supported by the fact that comparisons of results at larger values of $\bar{E}$ do show a decreasing trend (Fig. .9), although the magnitude of the rate of decrease is different as the values of $\bar{\delta}_{max}/\bar{\delta}_c$ in the current work are much greater than those used by Etsion et al. In summary, the current findings show that the accuracy of Eq. 6 is reduced outwith its calibration zone.

[Figure 9 about here.]

Considering next the empirical relations for unloading stiffness, Luding [13] and Walton and Braun [14] proposed linear relations for the increase of unloading stiffness with displacement and peak load, respectively. The linear relationship developed by Luding relating secant loading stiffness (k_1), secant unloading stiffness (k_2) and displacement is

$$k_2 = k_1 + (k_{2,max} - k_1)\,\frac{\delta_{max}}{\bar{\delta}_c^*} \tag{7}$$

where $\bar{\delta}_c^*$ it the transition displacement, which can be interpreted in physically meaningful terms as the displacement at first yield, $\bar{\delta}_c$ (Eq. 5). In terms of the quantities defined in the current the ratio of unloading to loading stiffness can be expressed as

$$\frac{k_2}{k_1} = \frac{F_{max}}{\delta_{max} - \delta_0} \cdot \frac{\delta_{max}}{F_{max}} = \frac{\bar{\delta}_{max}}{\bar{\delta}_{max} - \bar{\delta}_0} = \rho\bar{\delta}_{max} \tag{8}$$

Fig. .10 shows how the stiffness ratio obtained from FE simulations in the current work increases with relative displacement, for which the model of Luding [13] assumes linear relationships. Similarly, Fig. .11 shows the increase with maximum (dimensionless) load before unloading, for which the model of Walton and Braun [14] assumes linear relationships. Both figures show the limitations of using a linear model for unloading stiffness, even when the gradients are independently calibrated for each material. The results shown in Fig. .10 may be compared with the analytical and numerical findings of Rojek et al. [23], which, conversely, show that the linear relation of Luding is appropriate. However, it should be noted that a hardening plasticity model was used in this study with only a single set of parameters.

[Figure 10 about here.]

[Figure 11 about here.]

Results shown in Fig. .6 may also be compared with the relation proposed by Etsion et al. for displacement recovery, which was obtained by fitting FE results (Eq. 9),

$$\frac{1}{\rho} = \left[1 - \left(1 - \hat{\delta}^{-0.28}\right)\left(1 - \hat{\delta}^{-0.69}\right)\right]\bar{\delta}_{max}, \qquad (9)$$
$$\hat{\delta} = \frac{\bar{\delta}_{max}}{\bar{\delta}_c(\bar{E})}$$

[Figure 12 about here.]

where $\bar{\delta}_c$ is defined in Eq. 5. Eq. 9 predicts that the displacement recovered increases monotonically with $\bar{\delta}_{max}$ and $\bar{E}$, whereas the results shown in Fig. .6 show that at very high displacements, the proportion recovered after unloading starts to decrease. Simulations carried out in the current work found better agreement at the smallest displacements and smallest values of $\bar{E}$, but found significantly less elastic recovery following unloading (Fig. .12) for larger values, indicating the limited range of validity of Eq. 9. This discrepancy in results is not surprising: the range of values of $\hat{\delta}$ used in the six FE simulations described by Etsion et al. for calibration was $\hat{\delta} \leq 170$, whereas the smallest value represented in Fig. .12 is 366 ($\bar{E} = 200$, $\bar{\delta} = 0.01$) and the largest ($\bar{E} = 1000$, $\bar{\delta} = 0.5$) is 4.75×10^5.

Mesarovic & Johnson [8] proposed Eq. 10 to describe the relationship between load and area on unloading.

$$\frac{\bar{F}_{unl}}{\bar{F}_{max}} = \left(\frac{2}{\pi}\right)\left[\operatorname{asin}(\hat{a}) - a^*\sqrt{1 - \hat{a}^2}\right], \qquad (10)$$
$$\hat{a} = \frac{\bar{a}_{unl}}{\bar{a}_{max}}$$

[Figure 13 about here.]

Simulation results (Fig. .13) obtained at $\bar{\delta}_{max} = 0.5$ show that, for large displacements, the Mesarovic-Johnson relation remains a realistic model only for relatively low stiffness particles.

5. A concentric cylinder model for large-displacement contact

In this Section, an expression for sphere unloading stiffness is derived for a simplified analytical model in order to provide some insight into the results obtained from the finite element contact simulations presented previously. The problem is simplified by considering a half-sphere in contact with a rigid plane approximated with a number of elastic-perfectly plastic cylinders, concentric around the contact normal, which are free to slide axially with respect to neighbouring cylinders, without friction. In conjunction with use of linear strain, this results in axial strain being uniform along each cylinder. Radial expansion of the cylinders is ignored.

[Figure 14 about here.]

Assuming the particle shape at the start and end of the unloading process is a truncated sphere, as illustrated in Fig. .14, the axial position of a point on the sphere is given by Eq. 11.

$$z = \sqrt{R^2 - r^2} \tag{11}$$

The axial position of points in contact with the impacting surface is $R - \bar{\delta}R_0$. The volume lying under the contact area can be divided into a central cylindrical core, in which all material has yielded, surrounded by an elastic annulus. On the contact surface, plastic contact and total contact regions are delimited by the plastic radius r_p and the contact radius r_m, respectively. This description of contact behaviour with reference to concentric elastic and plastic contact zones is conceptually similar to that proposed by Vu-Quoc et al. [24]. From considering the deformed geometry (Fig. .14), elastic axial strain in the elastic region during both loading and unloading is given by Eq. 12.

$$\varepsilon_{e,e}(\bar{r}) = \frac{1-\bar{\delta}}{\sqrt{1-\bar{r}^2}} - 1, \qquad \bar{r}_p \leq \bar{r} \leq \bar{r}_m \tag{12}$$

In the subsequent development, symbols with a overbar represent quantities that have been nondimensionalised as described in Section 2.1.

The contact radius during both particle loading and particle unloading can be determined by setting elastic strain to zero (Eq. 13),

$$\bar{r}_m = \sqrt{2\bar{\delta} - \bar{\delta}^2} \tag{13}$$

Variation of the plastic radius during particle loading is found by equating elastic strain to yield strain (Eq. 14),

$$\bar{r}_p = \sqrt{1 - \left(\frac{\bar{E}(1-\bar{\delta})}{\bar{E}-1}\right)^2} \tag{14}$$

noting that yielding is never attained when $\bar{E} = 1$. During unloading, the plastic radius stays at the value calculated by evaluating Eq. 14 at $\bar{\delta} = \bar{\delta}_{max}$. The contact force can be determined by integrating the axial stress (Eq. 15).

$$F = \int_0^{r_p} 2\pi r \sigma_y \, \mathrm{d}r + \int_{r_p}^{r_m} 2\pi r E \varepsilon_e \, \mathrm{d}r \tag{15}$$

In dimensionless form, Eq. 15 becomes Eq. 16.

$$\bar{F} = 2\int_0^{\bar{r}_p} \bar{r} \, \mathrm{d}\bar{r} + 2\bar{E}\int_{\bar{r}_p}^{\bar{r}_m} \bar{r}\varepsilon_{e,e} \, \mathrm{d}\bar{r} \tag{16}$$

Using Eq. 12 with Eq. 16 results in

$$\begin{gathered}\bar{F}(\bar{\delta}) = \bar{r}_p^2 + \bar{E}(\bar{r}_m^2 - \bar{r}_p^2) + \\ 2\bar{E}(\bar{\delta}-1)\left[\sqrt{1-\bar{r}_p^2} - \sqrt{1-\bar{r}_m^2}\right]\end{gathered} \tag{17}$$

Elastic axial strain in the plastic region on unloading is obtained by adding to the yield strain (Eq. 18).

$$\varepsilon_{e,p}(\bar{r}) = -\frac{1}{\bar{E}} + \frac{\bar{\delta}_{max} - \bar{\delta}}{\sqrt{1-\bar{r}^2}}, \qquad 0 \le \bar{r} \le \bar{r}_p \tag{18}$$

while elastic strain in the unloading elastic region is the same as during loading (Eq. 12). The contact radius during unloading is the same as for loading, following the geometrical assumptions (Eq. 13), while the plastic radius stays at the maximum value. Force in unloading is then obtained by substituting Eqs. 12 and 18 into Eq. 16.

$$\bar{F}(\bar{\delta}) = \bar{r}_p^2 + 2\bar{E}(\bar{\delta}_{max} - \bar{\delta})\left(\sqrt{1-\bar{r}_p^2} - 1\right) + \\ \bar{E}(\bar{r}_m^2 - \bar{r}_p^2) + 2\bar{E}(\bar{\delta} - 1)\left(\sqrt{1-\bar{r}_p^2} - \sqrt{1-\bar{r}_m^2}\right) \tag{19}$$

Expanding and separating the terms that are constant in $\bar{\delta}$ simplifies to Eq. 20.

$$\bar{F} = \bar{E}\bar{\delta}^2 + \{\text{constants}\} \tag{20}$$

Eq. 20 can be expressed in terms of the dimensionelss load before unloading (Eq. 21),

$$\bar{F}_{unl} = \bar{F}_{max} - \bar{E}(\bar{\delta} - \bar{\delta}_{max})^2 \tag{21}$$

the exponent indicating that the unloading nonlinearity resulting from the analytical model is uniformly 2. By substituting $\bar{F}_{unl}(\bar{\delta}_0) = 0$ and definition of ρ, Eq. 1 into Eq. 21 and rearranging, an expression for the unloading stiffness is obained (Eq. 22).

$$\rho = \sqrt{\frac{\bar{E}}{\bar{F}_{max}}} \tag{22}$$

Using Eq. 22 and Eqs. 17 and 13 evaluated at $\bar{\delta} = \bar{\delta}_{max}$ allows ρ to be computed as an explicit function of $\bar{E}$ and $\bar{\delta}$ (Eqn. 23).

$$\rho = \sqrt{\frac{\bar{E}(\bar{E}-1)}{\bar{E}\bar{\delta}_{max}(2-\bar{\delta}_{max}) - 1}} \tag{23}$$

Full results for ρ are presented in Figs. .16 and .17. By comparing these figures with Figs. .5 and .6, it can be seen that similar general trends are shown in results from both analytical FE models. While the increase of secant stiffness with material stiffness is captured by the analytical model (though it is less pronounced), the decrease of secant stiffness at moderate values of displacement is captured by the analytical model, but increase in secant stiffness with $\bar{\delta}_{max}$ at high displacements is not captured. By plotting values of the dimensionless contact area $\bar{a}$ obtained from both analytical and FE models (Fig. .15), it can be seen that Eq. 13 becomes increasingly inaccurate at displacement of $\bar{\delta}_{max}$ greater that about 0.3. However, the magnitude of the ratio between in contact area prior to unloading obtained from FE simulations and that obtained from by the analytical model (≤ 1.24) is insufficient to explain the magnitude of the increases in secant stiffness observed in Fig. .6 (peak-to-trough ratios of 2.0 - 2.4 for $\bar{E} \geq 20$). Consequently, it is concluded that the tendency described in Section 4.4 of increasing contact load to drive stress states into hydrostatic compression is primarily responsible for restrictions in kinematic relaxation during unloading at high values of $\bar{\delta}_{max}$, leading to large increases in the secant unloading stiffness.

[Figure 15 about here.]

[Figure 16 about here.]

[Figure 17 about here.]

6. Discussion

In the current study, the von Mises metal plasticity model is used to describe the yielding behaviour of the particle material, which allows the material to be characterised with only three parameters. Nonmetallic particles typically demonstrate a degree of compaction (volumetric strain) due to contact, which are more accurately described by compressible plasticity models, such as the Drucker-Prager Cap model. Such materials may also show variation in Young's modulus due to compaction. Some unloading results for spherical particles were presented by Edmans and Sinka [27] but explicit relations for unloading stiffness for such particles, and a comparison with the findings of the current work, were not shown.

In large-scale DEM simulations, it might be desirable to implement only the stiffness property of the unloading response and use a linear unloading law. In this case, the values of k_2/k_1 charted in Fig. .10 may be considered for use in piecewise-linear normal contact laws as an alternative to Eq. 3.

The findings of this work may also be used to improve interparticle bond models including effects that are directly or indirectly dependent on elastic energy release rates, such as those including adhesion, rate-dependent effects and bond breakage.

7. Conclusions

In the current work, the load-displacement response of non-adhesive elastic-perfectly plastic spheres in unloading from contact was investigated using a systematic finite element study covering a more extensive space of material properties and deformation states than hitherto considered. The unloading curves were characterised by defining the (dimensionless) secant unloading stiffness of a particle as the reciprocal of dimensionless displacement recovered during unloading (Eq. 1), from which traditional forms of the unloading stiffness be calculated. Results obtained from the finite element study were used to formulate an empirical relation (Eq. 3) capable of accurately determining unloading stiffness (see Fig. .19) across the parameter space with only five parameters. Eq. 3 allows the unloading stiffness of a particle to be calculated directly, rather than requiring calibration, as for semi-empirical approaches [13, 14, 26]. This relation implies that unloading stiffness following plastic loading generally increases with dimensionless material stiffness ($\bar{E}$) and decreases with dimensionless displacement before unloading ($\bar{\delta}_{max}$), although a significant increase in unloading stiffness at large displacements is also observed. An analytical model based on simplified kinematics and aggregation of one-dimensional stress elements was used to support the claim that this increase in unloading stiffness is primarily a three-dimensional stress effect associated with reduction of kinematic relaxation from particle material with high hydrostatic stress, although the increased contact area at large displacements (see Fig. .15) also plays a role. The influence of Poisson's ratio on unloading stiffness was shown to be small, but not negligible. By using the current finite element results, the limitations of some empirical relations developed for unloading stiffness were demonstrated and charted (Figs. .10 and .11).

A characteristic feature of the unloading force-displacement curves determined in this study is their nonlinearity. Explanations for the source of this nonlinearity and were advanced in Section 4.4, with reference to contact area and three-dimensional stress effects. It was found that increasing material stiffness tended to drive unloading response from an elastic-type (with nonlinearity increasing with initial displacement) to a plastic-bar-type (with nonlinearity reducing to 1.0 with increasing displacement) response.

Several authors (for example, Etsion [21], Luding [13] and Mesarovic & Johnson [8]) have proposed using the ratio of displacement to critical displacement, $\bar{\delta}/\bar{\delta}_c$, as a measure of the effective magnitude of particle deformation and the degree to which the particle's deformation is "plastic" rather than elastic, and incorporate this measure into empirical relations. The current work shows that, at large initial displacements, trends in results with increasing dimensionless stiffness are qualitatively and quantitatively different to those with increasing initial displacement, and this is true for both secant unloading stiffness and unloading nonlinearity. This effect is shown most clearly in Fig. .10, where results distinguished by different stiffness ($\bar{E}$) are not collapse to a single curve defined by $\bar{\delta}/\bar{\delta}_c$. Consequently, this measure was found to be insufficient to characterise unloading response at large deformations across the parameter space investigated in this work, and therefore three independent arguments were necessary in the model equation (Eq. 3) developed.

In summary, the unloading of particles, with simplifying assumptions, presents systematic trends in behaviour that can be accurately approximated by analytical relations and explained with reference to physical mechanisms. The findings of this work are presented as a contribution to the development of simulation methods for particle mechanics.

Acknowledgments

This work was supported by the UK Engineering and Physical Science Research Council [project reference EP/N025261/1].

References

[1] P. Cundall, O. Strack, A discrete numerical model for granular assemblies, Geotechnique 29 (1) (1979) 47–65. doi:10.1680/geot.1979.29.1.47.

[2] J. Rojek, A. Zubelewicz, N. Madan, S. Nosewicz, The discrete element method with deformable particles, International Journal for Numerical Methods in Engineering 114 (8) (2018) 828–860. doi:10.1002/nme.5767.

[3] D. O. Potyondy, P. Cundall, A bonded-particle model for rock, International Journal of Rock Mechanics and Mining Sciences 41 (8) (2004) 1329 – 1364, rock Mechanics Results from the Underground Research Laboratory, Canada. doi:10.1016/j.ijrmms.2004.09.011.

[4] H. Hertz, Über die Berührung fester elastischer Körper., Journal für die reine und angewandte Mathematik (1882) 156–171.

[5] Y. Tatara, On compression of rubber elastic sphere over a large range of displacements-part 1: Theoretical study, Journal of Engineering Materials and Technology, Transactions of the ASME 113 (3) (1991) 285–291. doi:10.1115/1.2903407.

[6] R. Hill, The Mathematical Theory of Plasticity, Clarendon Press, Oxford, 1950.

[7] B. Storåkers, S. Biwa, P.-L. Larsson, Similarity analysis of inelastic contact, International Journal of Solids and Structures 34 (24) (1997) 3061 – 3083. doi:10.1016/S0020-7683(96)00176-X.

[8] S. Mesarovic, K. Johnson, Adhesive contact of elastic-plastic spheres, Journal of the Mechanics and Physics of Solids 48 (10) (2000) 2009–2033. doi:10.1016/S0022-5096(00)00004-1.

[9] M. Brake, An analytical elastic-perfectly plastic contact model, International Journal of Solids and Structures 49 (22) (2012) 3129–3141. doi:10.1016/j.ijsolstr.2012.06.013.

[10] M. Gonzalez, Generalized loading-unloading contact laws for elasto-plastic spheres with bonding strength, Journal of the Mechanics and Physics of Solids 122 (2019) 633 – 656. doi:/10.1016/j.jmps.2018.09.023.

[11] M. Pasha, S. Dogbe, C. Hare, A. Hassanpour, M. Ghadiri, A linear model of elasto-plastic and adhesive contact deformation, Granular Matter 16 (1) (2014) 151–162. doi:10.1007/s10035-013-0476-y.

[12] J. Tomas, Mechanics of particle adhesion 1, in: CHIS A2004, 16th International Congress of Chemical and Process Engineering, Prague, Czech Republic, 2006.

[13] S. Luding, Cohesive, frictional powders: Contact models for tension, Granular Matter 10 (4) (2008) 235–246. doi:10.1007/s10035-008-0099-x.

[14] O. Walton, R. Braun, Viscosity, granular-temperature, and stress calculations for shearing assemblies of inelastic, frictional disks, Journal of Rheology 30 (1986) 949. doi:10.1122/1.549893.

[15] S. Thakur, J. Morrissey, J. Sun, J. Chen, J. Ooi, Micromechanical analysis of cohesive granular materials using the discrete element method with an adhesive elasto-plastic contact model, Granular Matter 16 (3) (2014) 383–400. doi:10.1007/s10035-014-0506-4.

[16] C. Thornton, Coefficient of restitution for collinear collisions of elastic- perfectly plastic spheres, Journal of Applied Mechanics, Transactions ASME 64 (2) (1997) 383–386. doi:10.1115/1.2787319.

[17] C. Thornton, Z. Ning, A theoretical model for the stick/bounce behaviour of adhesive, elastic-plastic spheres, Powder Technology 99 (2) (1998) 154–162. doi:10.1016/S0032-5910(98)00099-0.

[18] W. J. Stronge, Impact Mechanics, 2nd Edition, Cambridge University Press, 2018. doi:10.1017/9781139050227.

[19] F. Li, J. Pan, C. Sinka, Contact laws between solid particles, Journal of the Mechanics and Physics of Solids 57 (8) (2009) 1194–1208.

[20] J. Alcalá, D. E. de los Ojos, Reassessing spherical indentation: Contact regimes and mechanical property extractions, International Journal of Solids and Structures 47 (20) (2010) 2714 – 2732. doi:10.1016/j.ijsolstr.2010.05.025.

[21] I. Etsion, Y. Kligerman, Y. Kadin, Unloading of an elastic-plastic loaded spherical contact, International Journal of Solids and Structures 42 (13) (2005) 3716–3729. doi:10.1016/j.ijsolstr.2004.12.006.

[22] E. Olsson, P.-L. Larsson, On force-displacement relations at contact between elastic-plastic adhesive bodies, Journal of the Mechanics and Physics of Solids 61 (5) (2013) 1185 – 1201. doi:10.1016/j.jmps.2013.01.004.

[23] J. Rojek, D. Lumelskyj, S. Nosewicz, B. Romelczyk-Baishya, Numerical and experimental investigation of an elastoplastic contact model for spherical discrete elements, Computational Particle Mechanics 6 (3) (2019) 383–392. doi:10.1007/s40571-018-00219-8.

[24] L. Vu-Quoc, X. Zhang, L. Lesburg, A normal force-displacement model for contacting spheres accounting for plastic deformation: Force-driven formulation, Journal of Applied Mechanics, Transactions ASME 67 (2) (2000) 363–371. doi:10.1115/1.1305334.

[25] S. P. Timoshenko, J. N. Goodier, Theory of Elasticity, McGraw-Hill, New York, 1970.

[26] W. R. Chang, I. Etsion, D. B. Bogy, Adhesion Model for Metallic Rough Surfaces, Journal of Tribology 110 (1) (1988) 50–56. doi:10.1115/1.3261574.

[27] B. Edmans, I. Sinka, Numerical derivation of a normal contact law for compressible plastic particles, Mechanics of Materials (2019) 103297doi:https://doi.org/10.1016/j.mechmat.2019.103297.

Appendix A. Full simulation results

[Figure 18 about here.]

[Figure 19 about here.]

[Figure 20 about here.]

[Figure 21 about here.]

[Figure 22 about here.]

List of Figures

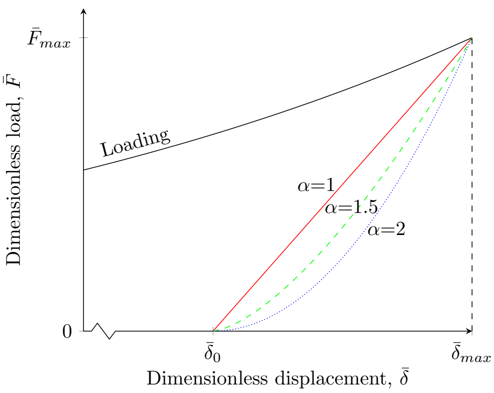

Figure .1: Sample unloading curves

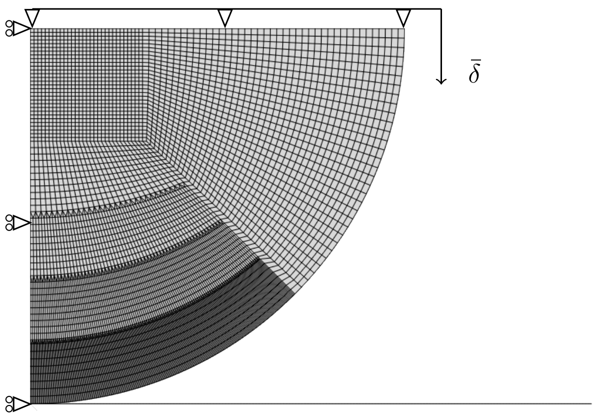

Figure .2: Finite element mesh with 6670 elements

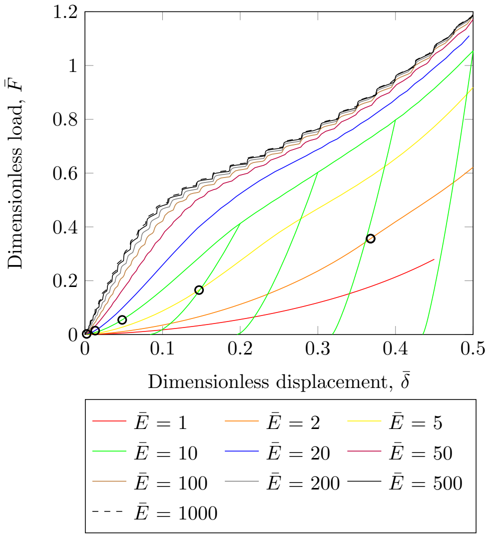

Figure .3: (Colour online) Load-displacement curves for loading with $\nu = 0.3$; selected unloading curves shown for $\bar{E}$=10. Circles show the point of first yield for each curve as calculated using Eq. 5.

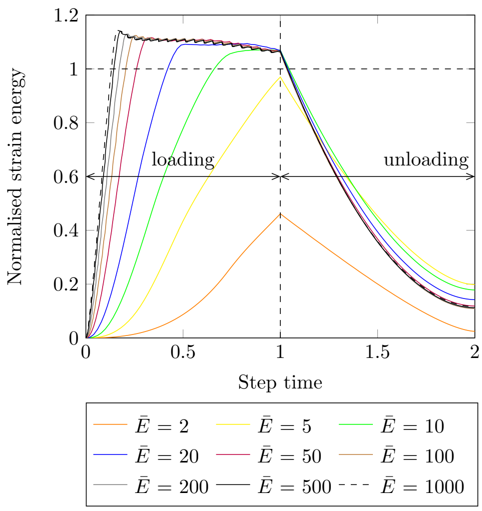

Figure .4: (Colour online) Strain energy in loading and unloading. All simulations loaded to $\bar{\delta}$=0.5. Strain energy is normalised with respect to maximum linear strain energy $((2/3)\pi R^3 \cdot (1/2)(\sigma_y^2/E))$. Values are greater that unity due to use of logarithmic strain in their calculation. Residual elastic strain at the end of the unloading step is primarily circumferential.

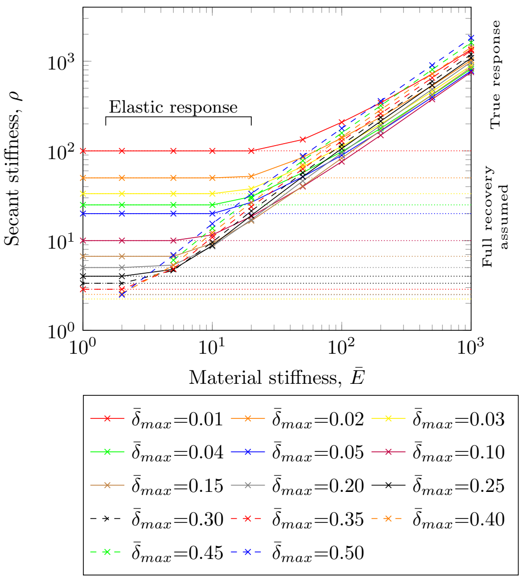

Figure .5: (Colour online) Relationship between $\bar{E}$ and secant stiffness ρ, lines for constant $\bar{\delta}_{max}$, for $\nu = 0.30$. Dotted continuation lines show values of ρ corresponding a fully elastic response for each value of $\bar{\delta}_{max}$.

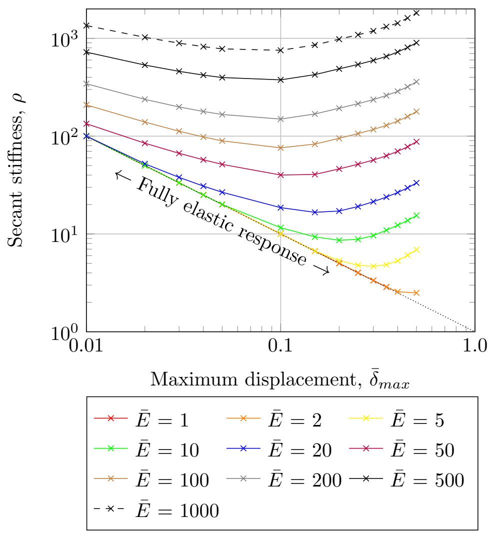

Figure .6: (Colour online) Relationship between $\bar{\delta}_{max}$ and ρ, lines for constant $\bar{E}$, for $\nu = 0.30$.

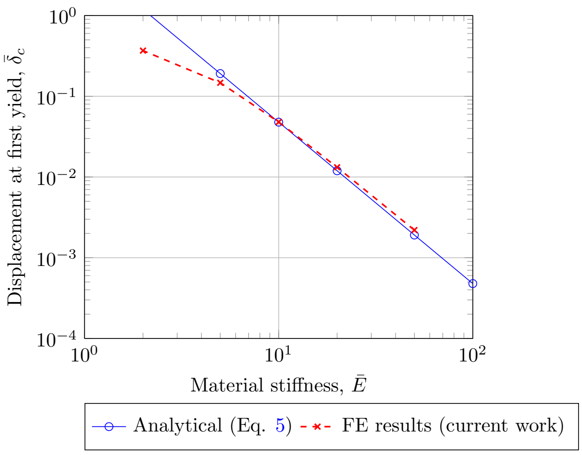

Figure .7: (Colour online) Comparison of Eq. 5 for predicting displacement at first yield with FE results for $\nu = 0.3$.

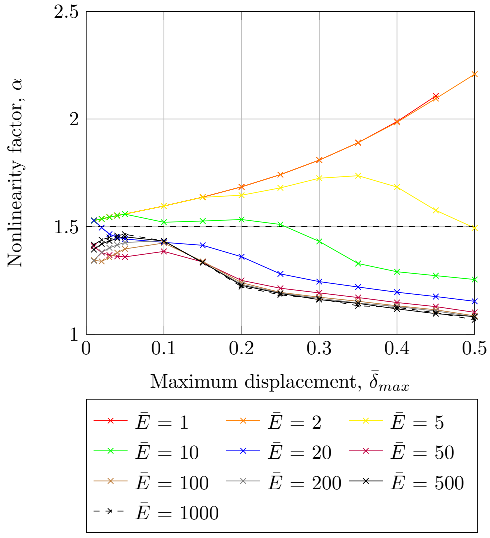

(a) Nonlinearity factor, $0 \leq \bar{\delta}_{max} \leq 0.5$, for $\nu = 0.30$

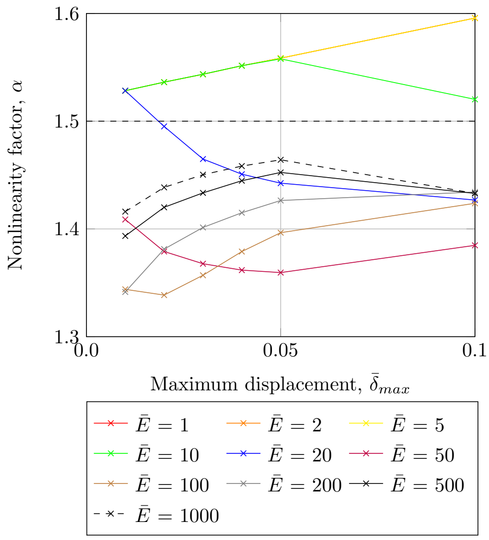

(b) Nonlinearity factor, $0 \leq \bar{\delta}_{max} \leq 0.1$, for $\nu = 0.30$

Figure .8: (Colour online) Values of the nonlinearity parameter α obtained from finite element simulations for $\nu = 0.30$, for (a) $0 \leq \bar{\delta}_{max} \leq 0.5$ (b) $0 \leq \bar{\delta}_{max} \leq 0.1$.

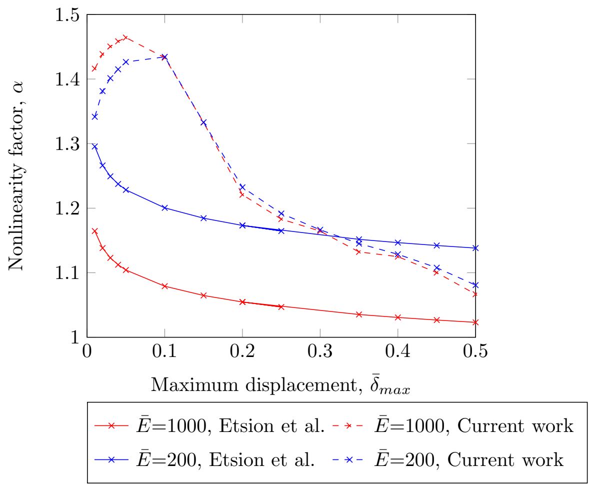

Figure .9: (Colour online) Comparison of α from FE simulations with relations proposed by Etsion et al. [21] (Eq. 6) for $\nu = 0.3$

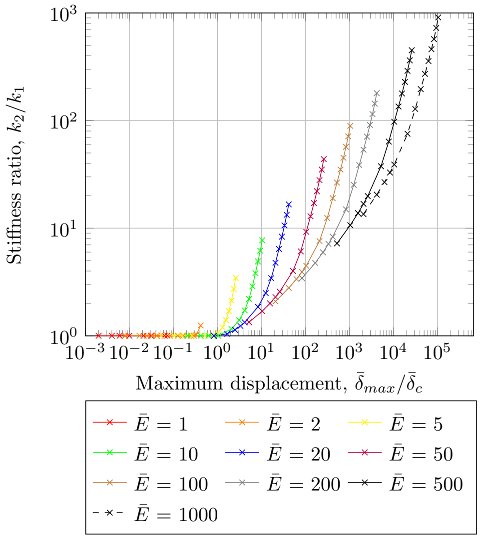

Figure .10: (Colour online) Relationship between $\bar{\delta}_{max}/\bar{\delta}_c$ and stiffness ratio k_2/k_1, lines for constant $\bar{E}$, for $\nu = 0.30$, for comparison with unloading model of Luding [13].

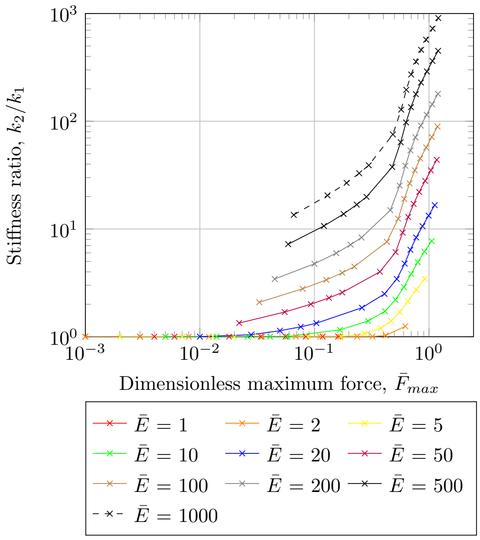

Figure .11: (Colour online) Relationship between $\bar{F}_{max}$ and stiffness ratio k_2/k_1, lines for constant $\bar{E}$, for $\nu = 0.30$, for comparison with the unloading model of Walton and Braun [14].

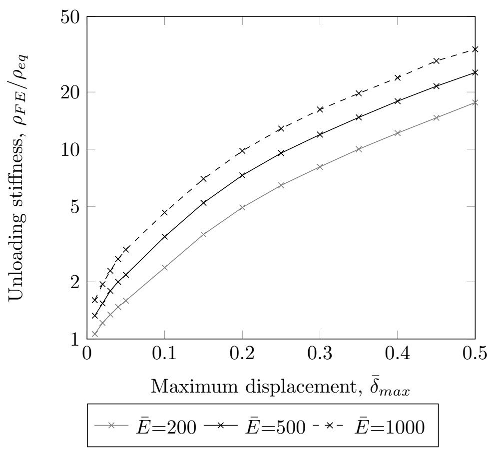

Figure .12: Ratio between unloading stiffness calculated from Eq. 9 (ρ_{eq}) and finite element results (ρ_{FE}) for $\nu = 0.3$.

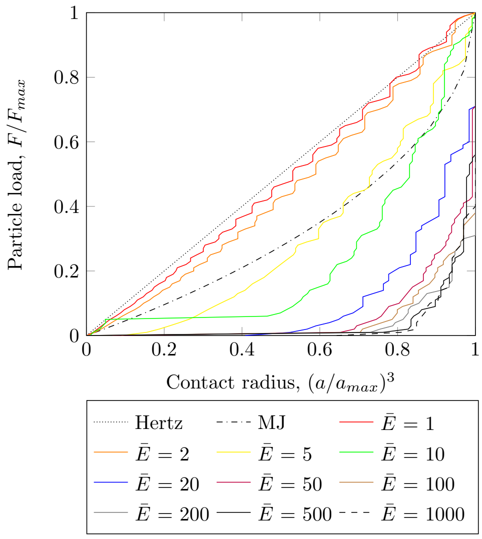

Figure .13: (Colour online) Relationship between particle load and contact area for $\nu = 0.3$. Anomalous behaviour was observed for $\bar{E}$=10 as secondary separation developed at the contact centre before unloading was completed.

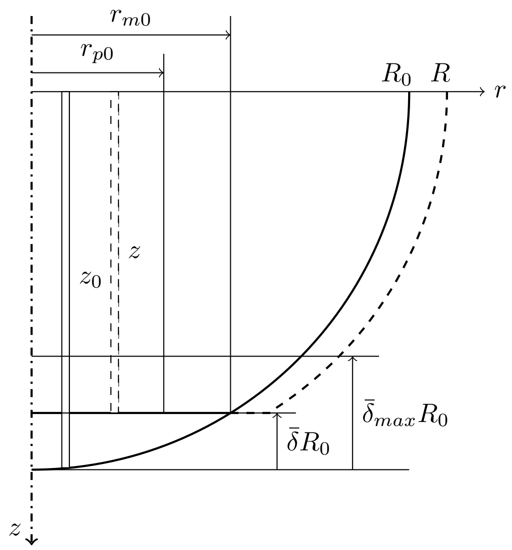

Figure .14: Geometry used in simplified model, showing cylindrical slices of differential width in undeformed (solid lines) and deformed (dashed lines) configurations. Quantities in the initial configuration are distinguished by a zero subscript; however, the distinction is not required by the current development.

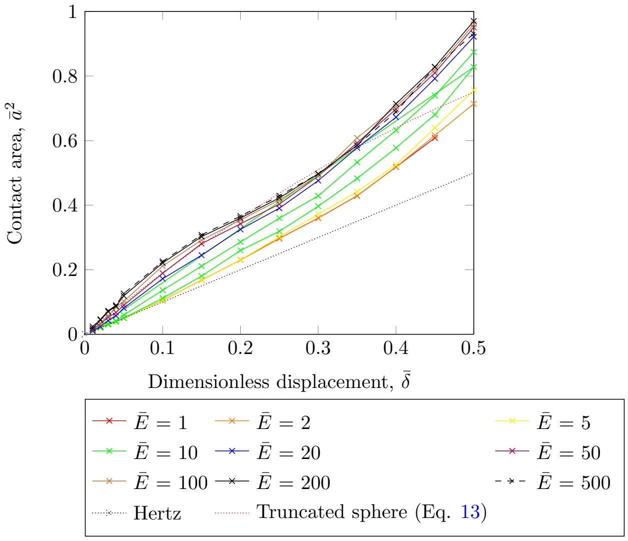

Figure .15: (Colour online) Contact area dependencies, $\bar{a} = \bar{a}(\bar{E}, \bar{\delta}_{max})$.

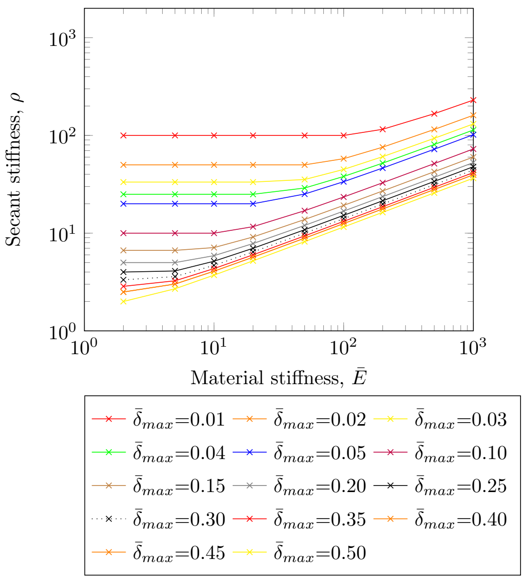

Figure .16: (Colour online) Relationship between $\bar{E}$ and secant stiffness ρ, lines for constant $\bar{\delta}_{max}$, for analytical model.

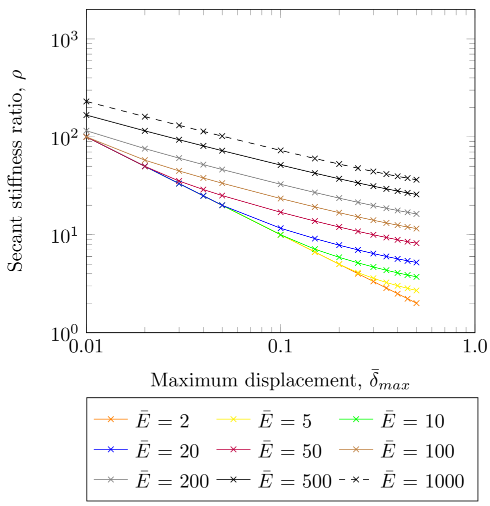

Figure .17: (Colour online) Relationship between $\bar{\delta}_{max}$ and ρ, lines for constant $\bar{E}$, for analytical model.

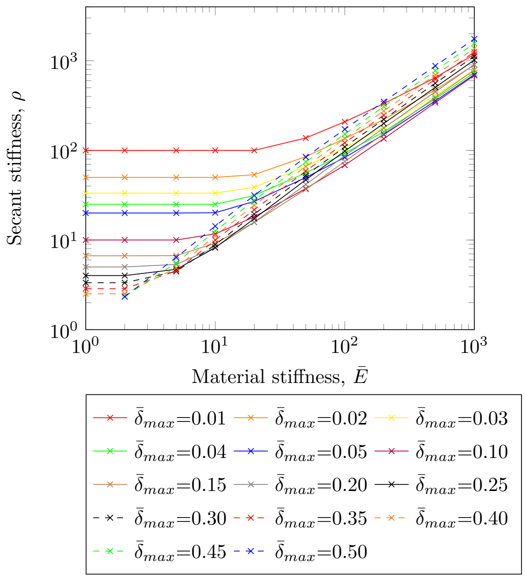

(a) $\rho(\bar{E}, \bar{\delta}_{max})$, ν=0.0

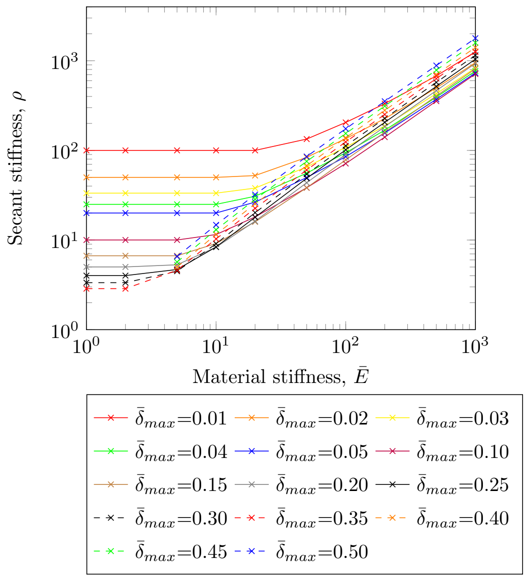

(b) $\rho(\bar{E}, \bar{\delta}_{max})$, ν=0.15

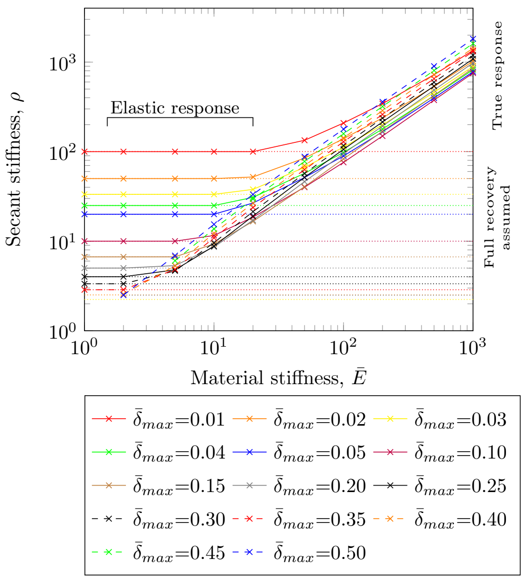

(c) $\rho(\bar{E}, \bar{\delta}_{max})$, ν=0.3

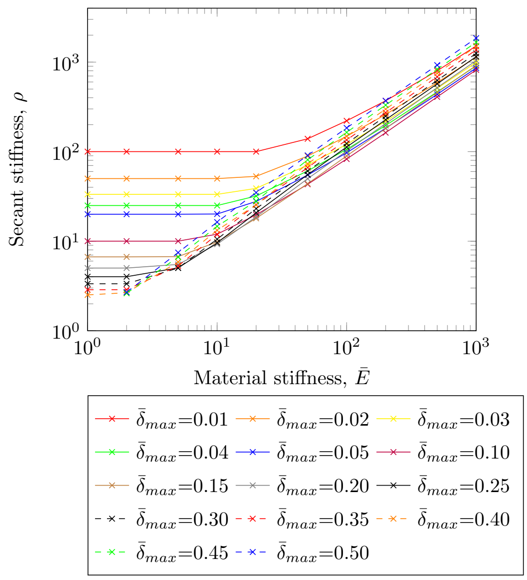

(d) $\rho(\bar{E}, \bar{\delta}_{max})$, ν=0.45

Figure .18: (Colour online) FE results showing relationship between $\bar{E}$ and secant stiffness ρ, lines for constant $\bar{\delta}_{max}$. (a) ν=0.0 (b) ν=0.15 (c) ν=0.30 (d) ν=0.45. Dotted continuation lines show values of ρ corresponding a fully elastic response for each value of $\bar{\delta}_{max}$.

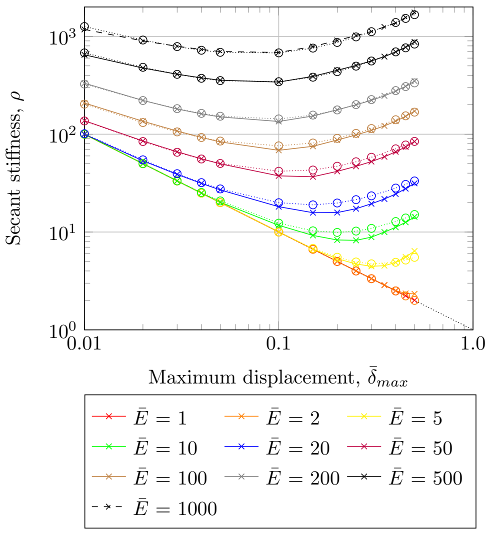

(a) $\rho(\bar{\delta}_{max}, \bar{E})$, ν=0.0

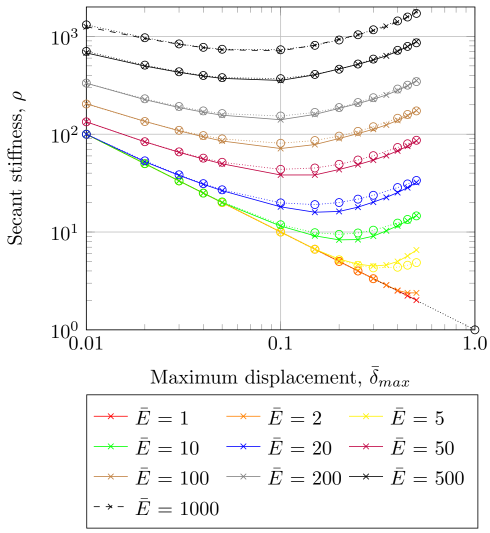

(b) $\rho(\bar{\delta}_{max}, \bar{E})$, ν=0.15

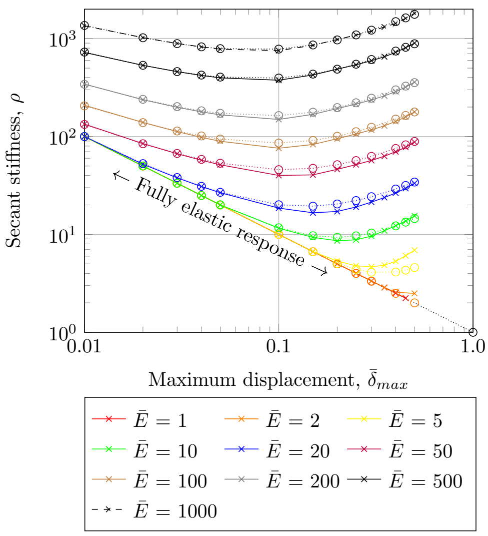

(c) $\rho(\bar{\delta}_{max}, \bar{E})$, ν=0.30

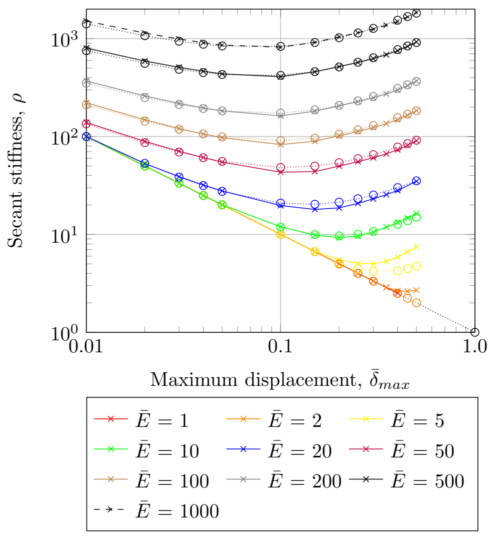

(d) $\rho(\bar{\delta}_{max}, \bar{E})$, ν=0.45

Figure .19: (Colour online) FE results showing relationship between $\bar{\delta}_{max}$ and secant stiffness ρ, lines for constant $\bar{E}$. (a) ν=0.0 (b) ν=0.15 (c) ν=0.30 (d) ν=0.45. Circles show values of ρ calculated with Eq. 3.

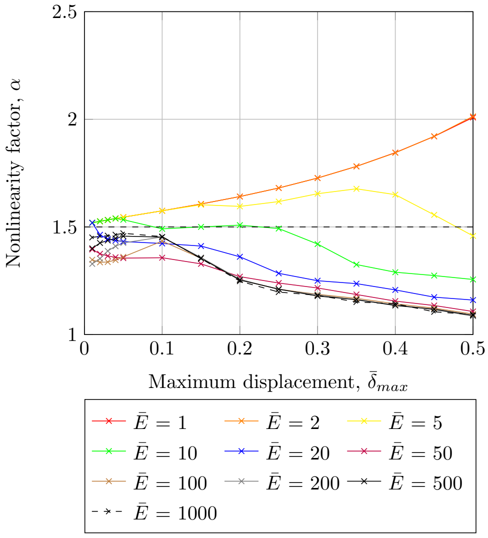

(a) $\alpha(\bar{E}, \bar{\delta}_{max})$, $\nu = 0.0$

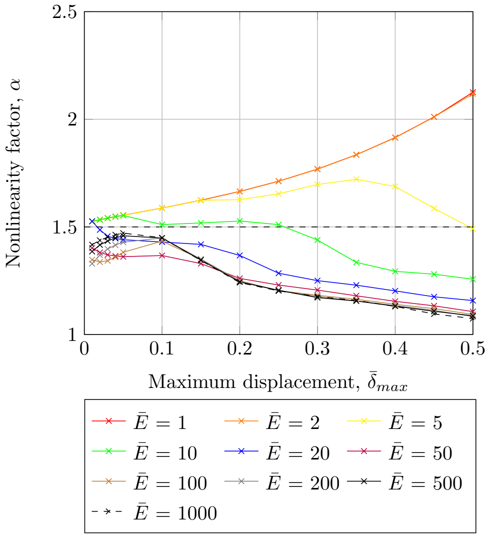

(b) $\alpha(\bar{E}, \bar{\delta}_{max})$, $\nu = 0.15$

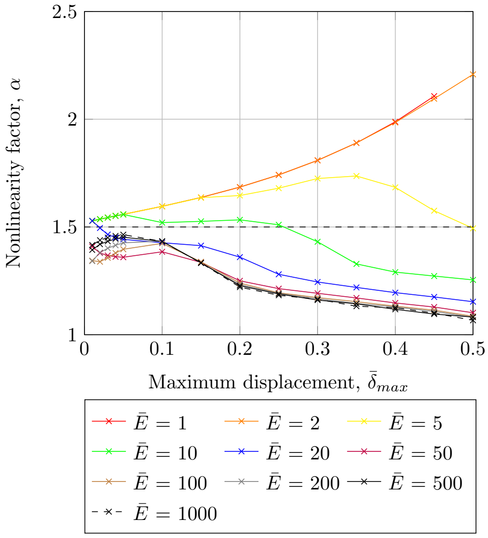

(c) $\alpha(\bar{E}, \bar{\delta}_{max})$, $\nu = 0.3$

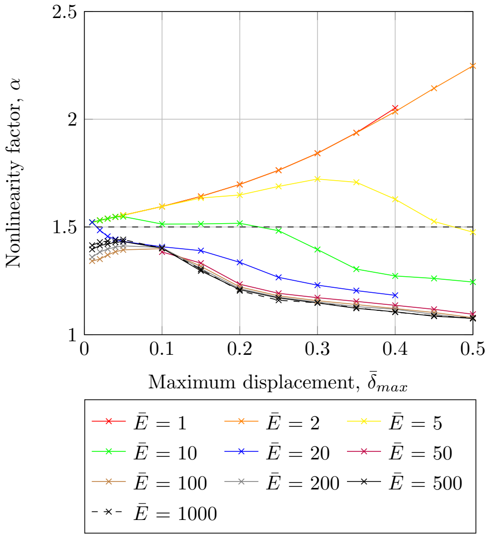

(d) $\alpha(\bar{E}, \bar{\delta}_{max})$, $\nu = 0.45$

Figure .20: (Colour online) FE results for unloading nonlinearity (a) ν=0.0 (b) ν=0.15 (c) ν=0.30 (d) ν=0.45.

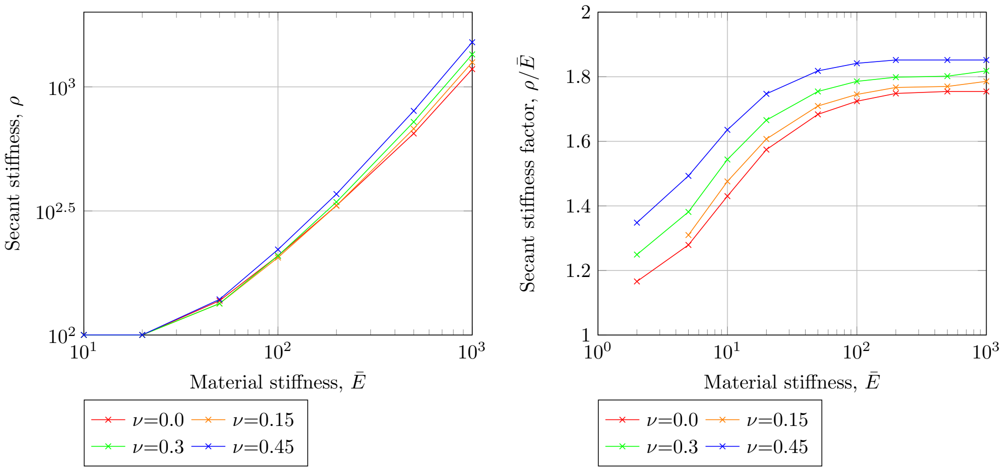

(a) $\rho(\bar{E}, \bar{\delta}_{max})$, $\bar{\delta}_{max}$=0.01

(b) $\rho(\bar{E}, \bar{\delta}_{max})/\bar{E}$, $\bar{\delta}_{max}$=0.5

Figure .21: Effects of ν on unloading stiffness (a) $\bar{\delta}_{max} = 0.01$ (b) $\bar{\delta}_{max} = 0.5$.

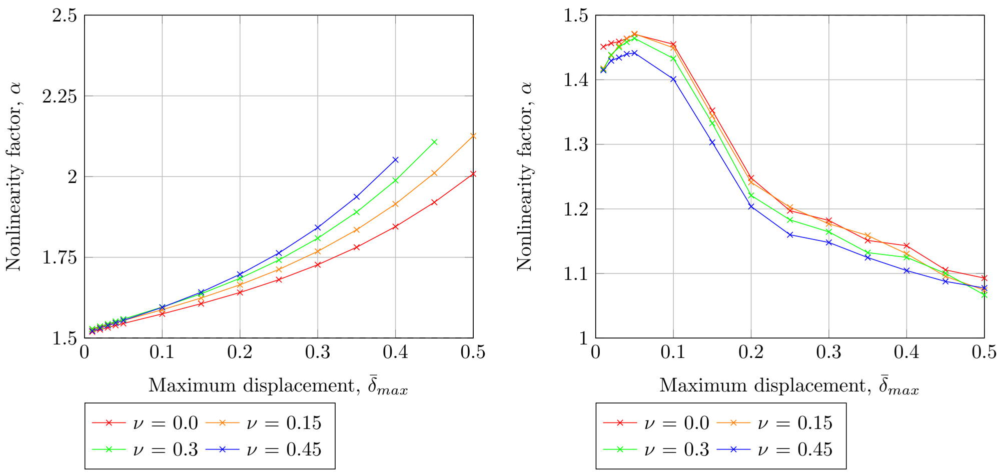

(a) $\alpha(\bar{E}, \bar{\delta}_{max})$, $\bar{E} = 1$

(b) $\alpha(\bar{E}, \bar{\delta}_{max})$, $\bar{E} = 1000$

Figure .22: Effects ν on nonlinearity (a) $\bar{\delta}_{max} = 0.01$ (b) $\bar{\delta}_{max} = 0.5$.

List of Tables

Parameter	Value
γ_1	2.9932
γ_2	0.1206
γ_3	0.4865
γ_4	0.2563
γ_5	0.3429

Table .1: Best-fit parameters for Eq. 3